12614 *Biochemistry* **2000,** *39,* 12614−12622

# Flexibility and Ligand Exchange in a Buried Cavity Mutant of T4 Lysozyme Studied by Multinuclear NMR[†]

Frans A. A. Mulder,[‡,§] Bin Hon,[§,||] D. Ranjith Muhandiram,[‡] Frederick W. Dahlquist,[||] and Lewis E. Kay*,[‡]

*Protein Engineering Network Centres of Excellence and Departments of Medical Genetics, Biochemistry, & Chemistry, University of Toronto, Toronto M5S 1A8, Ontario, Canada, and Institute of Molecular Biology & Department of Chemistry, University of Oregon, Eugene, Oregon 97403*

*Received June 13, 2000; Revised Manuscript Received August 3, 2000*

ABSTRACT: The Leu99→Ala mutant of T4 lysozyme contains a large internal cavity in the core of its C-terminal domain that is capable of reversibly binding small hydrophobic compounds. Although the cavity is completely buried, molecules such as benzene or xenon can exchange rapidly in and out. The dynamics of the unliganded protein have been compared to the wild-type protein by measuring the NMR spin relaxation rates of backbone amide and side chain methyl nuclei. Many residues surrounding the cavity were found to be affected by a chemical exchange process with a rate of $1500 \pm 200$ s$^{-1}$, which is quenched upon addition of saturating amounts of the ligand xenon. The relationship between the structure, dynamics, and energetics of the T4 lysozyme mutant is discussed.

An understanding of protein dynamics is critical for a complete description of many biological processes (*1*−*7*). Atom-specific information about structure and to a smaller extent flexibility has traditionally been derived from X-ray crystallography [see, for example, Huber (*2*) and Alber et al. (*3*)], which has revealed the importance of protein motion in processes such as enzyme catalysis. The modes, frequencies, and amplitudes of motions which occur on a time scale of several nanoseconds have been characterized in detail by molecular dynamics calculations (*5, 8*). In addition, high-resolution NMR has proven to be an extremely valuable tool for the study of protein internal dynamics at atomic resolution [reviewed by Wagner and Wüthrich (*9*), Palmer (*10*), Jardetzky (*11*), and Kay (*12*)]. In the past decade, a large number of NMR studies reporting on rapid (picosecond to nanosecond) backbone dynamics in proteins have appeared. The emerging picture is that for the most part these fast motions result in small (∼0.5 Å) excursions of backbone atoms from their mean positions in the protein. In contrast, far less is known about motions of side chains and dynamics occurring on longer (millisecond to microsecond) time scales that are likely responsible for binding and catalysis in many systems. For example, in the case of enzymes, substrate molecules require access to catalytic sites that can be partly or even completely buried. Transient conformational rearrangements are necessary to generate a path along which the substrate may enter into the binding pocket, involving the movement of both backbone and side chain atoms. Enzyme release rates for substrates consisting of 10−100 atoms have been measured to be $10-10^5$/s (*13*). Thus, the frequency of any required protein motion should coincide with or exceed these rates, yet little experimental data exist in this regard. One model for the study of the dynamics involved in binding of buried ligands is a Leu99→Ala mutant of T4 lysozyme which contains a large cavity capable of binding a number of ligands such as substituted benzenes and xenon (*14*, *39*, *40*, *51*). To what extent are motions on the $\mu$s−ms time scale available to the protein core of this cavity-containing mutant of T4 lysozyme? To answer this question, we have used a suite of NMR experiments measuring backbone $^{15}$N and side chain methyl $^{2}$H spin relaxation rates as well as experiments sensitive to backbone $^{1}$H and side chain methyl $^{13}$C and $^{1}$H spin relaxation to probe both fast (ps−ns) and intermediate ($\mu$s−ms) time scale dynamics throughout this molecule.

## MATERIALS AND METHODS

*Sample Preparation*.The three samples used in experiments, corresponding to wild type (WT),[1] recombinant cysteine-free T4 lysozyme (WT*, C54T/C97A), and L99A mutant (L99A with respect to WT*), were generated according to methods described (*15*). Uniformly $^{15}$N- and $^{15}$N/$^{13}$C-labeled proteins were produced in M9 media with $^{15}$NH$_4$Cl and $^{13}$C$_6$-glucose as sole nitrogen and carbon sources, respectively; 50% $^{2}$H-enriched samples were ob-

---

[†] This research was supported by grants from the Medical Research Council of Canada (L.E.K.), the Natural Sciences and Engineering Research Council of Canada (L.E.K.), and the National Institutes of Health (Grant GM57766) (F.W.D.). F.A.A.M. is a postdoctoral fellow with support from the Netherlands Organization for Scientific Research (NWO). L.E.K. is a foreign investigator of the Howard Hughes Medical Research Institute.

* Address correspondence to this author. 416-978-0741 (Phone), 416-978-6885 (Fax), Kay@pound.med.utoronto.ca (E-mail).

[‡] University of Toronto.

[§] Both authors contributed equally to this work.

[||] University of Oregon.

[1] Abbreviations: L99A, Leu→Ala99 substitution of WT* T4L; L99A+Xe, L99A with 60 psi xenon; ms, millisecond; ns, nanosecond; T4L, T4 lysozyme; $\mu$s, microsecond; WT, wild-type T4L; WT*, C54T, C97A T4L.

10.1021/bi001351t CCC: $19.00

tained from M9 media using a 1:1 volume ratio of $D_2O$/$H_2O$. Purified NMR samples were dialyzed into NMR buffer containing 50 mM sodium phosphate and 25 mM NaCl at pH 5.5. Sample concentrations were checked by UV absorbance at 280 nm and varied between 1.0 and 1.4 mM. Xe-binding experiments were performed using a model 524-PV-7 pressure NMR tube obtained from Wilmad Co.

*NMR Spectroscopy.* All NMR spectra were collected at 25 °C on Varian Inova 600 and UnityPlus 500 spectrometers. Backbone $^{15}$N,$^{1}$H and side chain methyl $^{13}$C,$^{1}$H resonance assignments of L99A and L99A under 60 psi xenon pressure were obtained primarily through analysis of 3D HNCACB, (H)CC(CO)NH-TOCSY, H(CC)(CO)NH-TOCSY, $^{15}$N-edited $^{1}$H-$^{1}$H NOESY, and $^{1}$H-$^{15}$N TOCSY-HSMQC experiments [reviewed by Sattler et al. *(16)*]. Previous assignments of wild-type T4 lysozyme *(17, 18)* were also helpful. Valine and leucine residues were discriminated in a correlation experiment that differentiates methyl groups on the basis of Val $\beta$ and Leu $\gamma$ $^{13}$C chemical shifts *(19)*. From this experiment, it was also possible to unambiguously assign Ile $\gamma_2$ and $\delta_1$ methyl resonances. Methionine methyl assignments were obtained from a long-range C−C coupling correlation experiment *(20)*. Stereospecific assignments of Val and Leu methyls were obtained by the method of Neri et al. *(21)*. Using this approach, complete assignments were obtained for the backbone amide and side chain methyl groups of WT and L99A lysozyme, the latter with and without 4 bar (60 psi) xenon.

Backbone dynamics were investigated by measuring amide $^{15}$N $T_1$, $T_2$ and $^{15}$N{$^{1}$H} NOE values as described previously (*22*). Side chain methyl deuterium $T_1$ and $T_{1\rho}$ values were obtained from the relaxation of $I_ZC_ZD_Z$, $I_ZC_ZD_Y$, and $I_ZC_Z$ operators, as described by Muhandiram et al. (*23*). Backbone and side chain relaxation measurements were acquired at 600 MHz using 100% $^{15}$N/$^{13}$C, 50% $^{2}$H labeled samples, unless stated otherwise. The $^{15}$N relaxation data have been submitted to the Indiana Dynamics Database at the University of Indiana (http://pooh.chem.indiana.edu/IDD.html). $^{15}$N-$^{1}$H CPMG-HSQC and reference HSQC experiments were acquired as described in Mulder et al. (*24*), by placing the $^{1}$H and $^{15}$N carrier frequencies in the center of the amide spectrum and suppressing the solvent signal by a selective off-resonance pulse at the beginning of the pulse sequence, followed by a gradient. $^{13}$C-$^{1}$H CT-CPMG-HSQC and reference HSQC experiments were acquired by placing the $^{1}$H and $^{13}$C carrier frequencies in the center of the methyl region (CPMG-HSQC pulse sequences have been deposited at the BioMagResBank http://www.bmrb.wisc.edu). $^{15}$N CPMG $R_2$ experiments with variable CMPG-delays were performed as described previously (*25*) on $^{15}$N-labeled samples of WT* and L99A, while all other experiments were recorded on samples of WT or L99A. All data were processed and analyzed using NMRPipe (*26*).

*Analysis of Backbone and Side Chain Dynamics.* Backbone and side chain relaxation rates were determined by fitting the intensities in the spin relaxation experiments described above to a single exponential as a function of the relaxation delay. Prior to extraction of parameters describing local backbone motions, a diffusion tensor analysis was carried out using the crystal structure of L99A [pdb entry code 1L90 (*27*)]. (A similar analysis was performed for data recorded on WT.) Optimization of the diffusion tensor parameters and the identification of residues that undergo chemical exchange were carried out as follows: Initially all the residues in the protein for which relaxation data were obtained were included in the calculation of the diffusion tensor (*28*) followed by model-free analysis (*29*, *30*) during which residues with $R_{ex}$ were identified. These residues were subsequently eliminated from the next iteration step, and the process was repeated until no residues with $R_{ex} > 1\ s^{-1}$ were obtained in the model-free analysis step. The results from the final trimmed data set indicate that L99A is best approximated by a prolate with a ratio $D_{par}/D_{per} = 1.32$ of the principal components $D_{par} = D_{ZZ}$ and $D_{per} = D_{XX} = D_{YY}$ of the axially symmetric diffusion tensor. Large reductions in the error function $\chi^2$ describing the agreement between experimental and calculated relaxation values were obtained when anisotropic models for the diffusion tensor were employed relative to a model based on isotropic tumbling. $F$-statistics were used to compare whether the improvement in the fit with additional parameters was indeed significant. The probability $p$ that the improvement using an axially symmetric diffusion tensor was due to chance was less than $10^{-10}$ ($F = 88$, 118 residues); a further decrease in $\chi^2$ upon including a rhombic term was not considered significant ($F = 2.7$, $p = 0.07$). Analysis of side chain relaxation data was performed as described previously (*23*).

$^{15}$N CPMG $R_2$ values were measured as a function of the $^{15}$N 180° pulse spacing, $2\tau_{cp}$, as described previously (*22*, *31*) with low-power $^{15}$N 180° pulses (127 $\mu$s) employed to avoid sample heating. The relaxation dispersion was fitted as a function of the average rf field, $\nu_{CPMG} = (4\tau_{cp})^{-1}$, using equations applicable to two-site fast exchange: $R_2 = R_2(\nu_{CPMG} = \infty) + R_{2,ex}$, where $R_{2,ex} = p_A p_B \delta\omega^2 \tau_{ex}[1 - 4\nu_{CPMG}\tau_{ex} \tanh(4\nu_{CPMG}\tau_{ex})^{-1}]$ (*25*, *32*), where $p_i$ is the fractional population of site i, $\delta\omega$ is the difference in the resonance frequencies of nuclei at the two sites expressed in angular frequency units, and $\tau_{ex}$ is the exchange correlation time, related to the forward ($k_1$) and backward ($k_{-1}$) rate constants by $\tau_{ex} = (k_1 + k_{-1})^{-1}$. The statistical significance of including the $R_{2,ex}$ exchange term in the fit of the dispersion data (i.e., one versus three parameters) was based on $F$-test criteria, treating a probability that the improvement is due to chance as significant if it is less than 0.05. Relaxation rates at $\nu_{CPMG} = 0$ (free precession limit) for each $^{15}$N spin were calculated from $^{15}$N line widths in a refocused HSQC with decoupling in $t_1$ achieved using the DIPSI-3 scheme (*33*). The line widths were obtained from line shape analysis in the frequency domain (*26*). A contribution of ~3 Hz to the line width due to inhomogeneity and incomplete decoupling was obtained for resonances without exchange (calculated by comparing the measured line width with the line width predicted from fitting of the relaxation rates) and consequently accounted for in the analysis (*34*).

## RESULTS AND DISCUSSION

*Engineered T4 Lysozyme Contains an Internal Cavity Capable of Binding Ligands.* The protein T4 lysozyme (T4L) has been extensively studied as well as engineered. The structures of a large number of T4L variants have been determined by X-ray crystallography, and have been complemented by thermodynamic studies of their stability to global unfolding (*35*−*38*). Various cavity-containing forms have

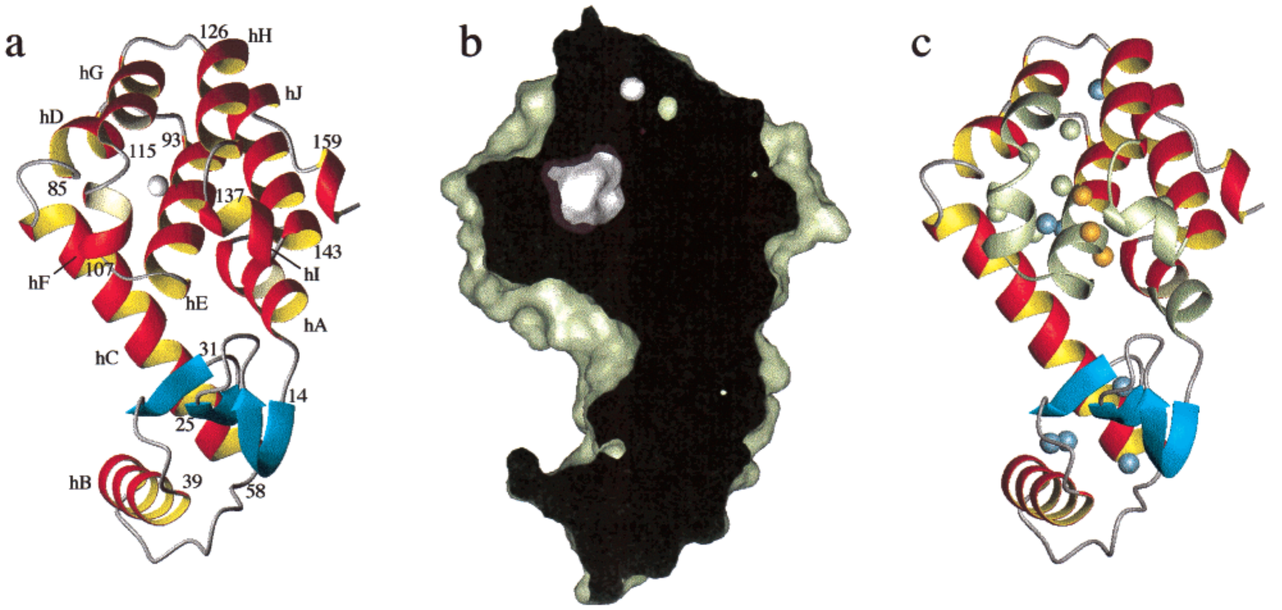

FIGURE 1: Three-dimensional representations of L99A T4 lysozyme. (a) Schematic ribbon representation. The helices and residues at the start of secondary structural elements have been labeled to facilitate the discussion in the text. The Ala99 C$\beta$ methyl carbon is shown as a white sphere. (b) Cross section through a space-filling representation. The continuous van der Waals surface, drawn with a 1.4 Å probe radius, is cut by the plane of the paper. All atoms shown lie behind the black plane, with the outside surface of the protein colored green and the internal cavities shown in white. The larger white surface affords a view down into part of the internal cavity of ~150 Å$^3$ that is formed by the Leu99→Ala substitution (*35*). The van der Waals surface at the bottom of the cavity is made up by the side chain of Tyr88. Other residues that are in close contact with the cavity include Ile78, Leu84, Val87, Leu91, Ala99, Val103, Leu118, and Phe153. (c). Schematic ribbon representation highlighting the locations in the protein where fast and intermediate time scale motions have been identified. Contiguous segments of the backbone that are affected by conformational exchange are colored green. Side chain methyl groups for which $\mu$s−ms time scale dynamics have been detected at carbon (proton) nuclei are shown as green (orange) spheres, while those for which increases in ps−ns time scale dynamics have been noted are highlighted in blue. Figure prepared with MOLMOL (*55*).

been created that can bind small, mostly hydrophobic compounds, such as substituted benzenes and xenon (*39*, *40*, *51*). The cavity mutant used in this study, L99A, has the substitution Leu→Ala at position 99 which results in strongly reduced thermal stability [$\Delta\Delta G_{\mathrm{unfolding}}$ at 44 °C = −5.0 kcal/mol and $\Delta T_{\mathrm{m}} = -15.7$ °C (*27*)]. Recent NMR studies have established that the off rates for binding of benzene and indole to L99A are rapid, on the order of 300 and 800 s$^{-1}$, respectively, at 20 °C (*14*). Truncation of the side chain, by the equivalent of three methylene groups, leaves the structure virtually unaltered relative to wild type (WT), and enlarges a preexisting completely buried internal cavity to about 150 Å$^3$ (*27*). Figure 1 shows a schematic overview of the protein topology, illustrating that it is comprised of two domains. A cross section through a space-filling model of the protein reveals the large internal, buried cavity present in the structure of L99A. Crystallographic temperature factors for WT and L99A (taken from pdb entry codes 6LZM and 1L90, respectively) are essentially the same and are low for the majority of the residues in the cavity-containing C-terminal lobe (*27*, *41*, *42*). Thus, insight into the dynamic processes required for ligand exchange in the L99A variant is difficult to obtain from static three-dimensional structures of these molecules.

*Conformational Exchange Affects an Extensive Portion of the Protein Surrounding the Cavity.* The internal dynamics of WT, L99A, and L99A saturated with respect to chemical shift changes by the addition of xenon (4 bar/60 psi xenon pressure, denoted by L99A+Xe in what follows) have been investigated on a per residue basis by NMR spin relaxation to obtain a description of internal flexibility on fast and intermediate time scales. To generate as complete a picture as possible, the relaxation of a large set of spin probes was monitored, including $^{15}$N and $^{1}$H spins of backbone amide groups and $^{1}$H, $^{2}$H, and $^{13}$C spins of methyl side chains.

Qualitative information about the presence of protein flexibility is readily obtained by comparing correlations in 2D $^{15}$N-$^{1}$H HSQC spectra. Motions of amide bonds occurring on the picosecond to nanosecond time scale that are of significant amplitude result in sharp resonance lines. On the other hand, motions on the millisecond to microsecond time scale which modulate the chemical shift environment of nuclei lead to broad and weak resonance lines. These so-called "chemical exchange" processes also result in a decrease in efficiency of polarization transfer steps in NMR experiments (*24*, *43*) and hence a decrease in signal intensity. Figure 2a−c shows portions of 2D $^{15}$N-$^{1}$H HSQC spectra obtained for WT, L99A, and L99A+Xe, respectively. Clearly, some of the resonances in the spectrum of the Leu99→Ala mutant are very weak relative to the corresponding peaks in WT, providing the first line of evidence for the presence of relatively slow internal motions. Figure 2d shows that the $^{15}$N transverse relaxation rate ($R_2$) for Thr142 is indeed increased significantly. To obtain a more quantitative picture of the backbone dynamics of WT and mutant protein, $^{15}$N $R_1$, $R_2$ and heteronuclear $^{15}$N{$^{1}$H} NOE values were measured for the three samples. A comparison of $^{15}$N order parameters, measuring the amplitude of the amide N−H bond vector motion, establishes that there is essentially no change in the fast backbone dynamics between WT and L99A. T4 lysozyme forms a very rigid scaffold with increased ps−ns dynamics only at the termini (Asn2 and Leu164) and two loop residues (Ser38 and Ser136). Tyr139 is the only residue which is slightly more dynamic after

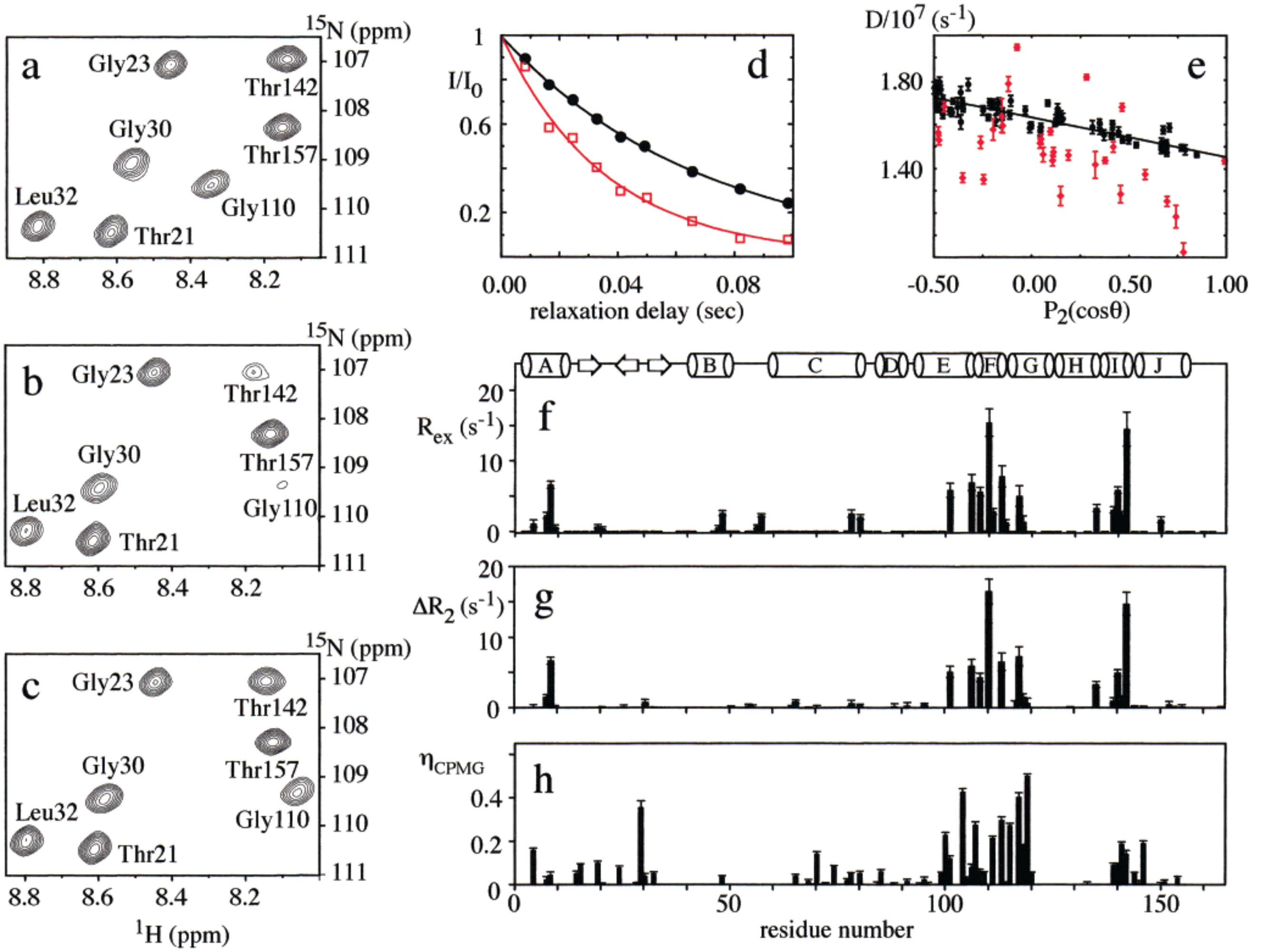

FIGURE 2: Exchange contributions to backbone $^{15}$N and $^{1}$H transverse relaxation rates for L99A. Panels a, b, and c show portions of 2D $^{15}$N-$^{1}$H HSQC spectra obtained for WT, L99A, and L99A+Xe, respectively. (d) $^{15}$N $R_2$ relaxation curves for Thr142 in WT (black filled circles) and L99A (red open squares). (e) Plot of calculated local diffusion constants $D$ per residue in L99A as a function of the orientation of the N−H bond vector in the frame of the axially symmetric diffusion tensor. Points which were included (excluded) from the calculation of the diffusion tensor are shown in black (red). The solid line illustrates the dependence of $D$ on N−H bond vector orientation for rigid body motion: $D = (^{1}/_{3}D_{\mathrm{par}} + {}^{2}/_{3}D_{\mathrm{perp}}) - {}^{1}/_{3}P_2(\cos\theta)(D_{\mathrm{par}} - D_{\mathrm{perp}})$. Points below (above) the line represent residues in regions of the protein that experience $\mu$s−ms (ps−ns) time scale dynamics. (f) Values of the fitted $R_{\mathrm{ex}}$ contributions obtained from the model-free analysis of the $^{15}$N backbone relaxation data for L99A. A diagram of secondary structural elements is provided at the top of the panel. (g) Residue-specific differences of $^{15}$N $R_2$ relaxation rates between L99A and WT: $\Delta R_2 = R_2^{\mathrm{L99A}} - R_2^{\mathrm{WT}}$. (h) Enhancement factors obtained from a comparison of spectra recorded on L99A with CPMG-INEPT- and free-precession INEPT-$^{15}$N-$^{1}$H HSQC pulse schemes. Large values of $\eta_{\mathrm{CPMG}}$ indicate exchange contributions to the $^{1}$H line width.

creating the cavity, but this mobility is quenched by the binding of xenon (see below).

Intermediate time scale dynamics were detected by calculating the excess contributions to the transverse relaxation rate of $^{15}$N nuclei, arising from time-dependent perturbations of the chemical shift (*44*). Since a large value of the $^{15}$N $R_2$ may also result from nonisotropic molecular tumbling (*45*), contributions from chemical exchange, $R_{\mathrm{ex}}$($^{15}$N), were extracted by an optimization procedure in which elements of the diffusion tensor and per-site motional parameters were calculated in an iterative manner as described under Materials and Methods. Figure 2e shows the per-residue diffusion constant, $D$, for L99A plotted as a function of N−H bond vector orientation. Residues in black were used in the final iteration to obtain the values of the diffusion tensor, while those in red correspond to residues with increased ps−ns (above the line) or $\mu$s−ms (below) time scale motion. Upon including anisotropic tumbling into the model-free analysis (*30*), exchange contributions were small [$R_{\mathrm{ex}}$($^{15}$N) < 2.1 s$^{-1}$] but measurable for a number of residues in WT. In the case of L99A, many residues required the inclusion of a large $R_{\mathrm{ex}}$ term in the model-free analysis, as shown in Figure 2f. Residues Phe4, Leu7, Arg8, Lys48, Val57, Ile78, Arg80, Asn101, Met106, Glu108, Gly110, Val111, Gly113, Phe114, Ser117, Leu118, Arg119, Lys135, Tyr139, Asn140, Gln141, Thr142, and Ile150 have significant $R_{\mathrm{ex}}$ values, indicating that they are affected by intermediate time scale motions. It is noteworthy that residues in helices E, F, and I are strongly influenced by exchange in L99A with the effects of exchange significantly reduced but not eliminated for some residues in these helices in the WT structure. $R_{\mathrm{ex}}$($^{15}$N) contributions that either are a direct consequence of the introduction of the cavity or are significantly influenced by the cavity could be identified directly from the increase in the values for $^{15}$N $R_2$ for L99A relative to WT, $\Delta R_2$, since WT and L99A have the same 3D structure (*35*) (Figure 2g). Positive excursions from the baseline indicate increased millisecond to microsecond time scale dynamics in L99A and correspond for the most part to the same residues identified from the diffusion tensor analysis, summarized in Figure 2f. Note that $R_{ex}(^{15}N)$ values for residues Lys48, Val57, Ile78, Arg80, and Ile150 (Figure 2f) are probably not a direct result of the cavity, since they do not contribute to $\Delta R_2$, but arise from other slow dynamic processes present in both WT and L99A. Interestingly, residues 57, 78, and 80 are situated at the "hinge" regions between the two domains, which have been previously implicated in domain–domain motion (*46*).

In addition to the $^{15}N$ spin relaxation experiments described above which are sensitive to magnetic field fluctuations at amide nitrogen positions, contributions to relaxation of amide protons from exchange have been qualitatively assessed by $^{15}N$-$^{1}H$ CPMG-HSQC experiments (*24, 47*). In these experiments, a pulse train of variable repetition rate is incorporated into the heteronuclear polarization transfer steps of the HSQC experiment, and the resultant spectral intensities encode $^1H$ transverse relaxation contributions due to conformational exchange, $R_{ex}(^1H)$. The enhancement of the signal by CPMG-INEPT ($I_{CPMG}$) relative to free precession INEPT-based HSQCs is expressed as $\eta_{CPMG} = (I_{CPMG} - I_{HSQC})/I_{HSQC}$, and values of $\eta_{CPMG} > 0$ indicate millisecond to microsecond time scale dynamics. The enhancement factors obtained for the backbone amide protons of L99A are presented in Figure 2h. Large values of $\eta_{CPMG}$ (>0.13) indicate $R_{ex}(^1H)$ for residues Phe4, Ile29, Asp70, Ile100, Phe104, Gly107, Val111, Gly113, Thr115, Ser117, Leu118, Arg119, Gln141, Thr142, and Ala146. Not surprisingly, these experiments identify intermediate time scale dynamics in the same region of the protein as found from $^{15}N$-based relaxation experiments. The combined analysis is, however, more complete since it is possible to gain insight into the origins of the modulation of the chemical shift (*47, 48*) (see below).

Side chain dynamics were also probed by both approaches, including methyl $^2H$ $R_1$ and $R_{1\rho}$ relaxation (*23*) and $^{13}C$-$^1H$ CPMG-HSQC experiments. Since the cavity in L99A is lined predominantly with methyl-containing side chains, changes in the relaxation rates of methyl-bound spins present a highly valuable diagnostic of dynamic changes in the protein core as a result of the amino acid substitution. Information about slow motions involving methyl side chains can be obtained from the disappearance of spectral peaks due to chemical exchange in 2D $^{13}C$-$^1H$ correlation maps obtained from experiments used to measure the decay of longitudinal order, $I_ZC_ZD_Z$ (*23*), as shown in Figure 3a–c. Again, as a result of slow motions, resonances are weak or missing due to broadening of the peaks by increased relaxation rates of methyl $^1H$ and/or $^{13}C$ spins, combined with compromised magnetization transfer efficiencies. Strongly reduced intensities were observed for several methyl groups in a comparison of 2D $^{13}C$-$^1H$ correlation maps used to measure the decay of $I_ZC_ZD_Z$ and $I_ZC_Z$ terms. In principle, in the absence of relaxation, spectra used to record the relaxation of $I_ZC_ZD_Z$ should be reduced in intensity by a factor of 4/9 relative to the corresponding spectra measuring the decay of $I_ZC_Z$ since the former experiment involves further transfers to and from $^2H$. However, because the $I_ZC_ZD_Z$ experiment has an additional delay of $\tau = 29$ ms, the sensitivity of the experiment will be reduced further by the factor $\exp(-R_2\tau)$, where the $^{13}C$ relaxation rate $R_2$ is dominated by dipole–dipole relaxation and chemical exchange terms. Contributions from dipolar relaxation reflect fast (ps–ns) time scale dynamics and can lead to intensity variations of as large as ~30% in cross-peaks for different $^1H$-$^{13}C$ methyl spins. In Figure 3d, the ratios of cross-peaks obtained in the $I_ZC_Z$ experiment relative to those from the $I_ZC_ZD_Z$ experiment ($\eta_{ZZZ}$) are plotted as a function of residue number for L99A. The majority of residues are a factor of 3 more intense in the $I_ZC_Z$ experiment, as expected. However, large differences are observed for certain methyl correlations resulting from exchange contributions to the $^{13}C$ methyl relaxation. Specifically, Leu84$\delta_1$, Ala99$\beta$, Val103$\gamma_2$, Leu118$\delta_2$, Leu121$\delta_1$, and Ala146$\beta$ are affected by millisecond to microsecond time scale motions. It is noteworthy that, with the exception of Ala146, all of these residues are in proximity to the cavity.

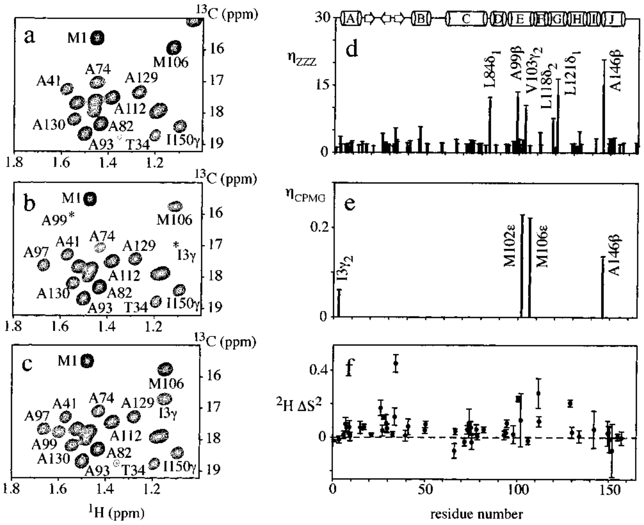

FIGURE 3: Side chain methyl dynamics in L99A. Panels a, b, and c show portions of the methyl regions of 2D $^{13}C$-$^1H$ HSQC spectra obtained for WT, L99A, and L99A+Xe, respectively. In (b), cross-peaks below the threshold plotted are denoted by *. (d) Intensity ratio ($\eta_{ZZZ}$) of 2D cross-peaks in $^{13}C$-$^1H$ HSQC spectra of L99A recording the decay of $I_ZC_Z$ and $I_ZC_ZD_Z$ components, respectively, at zero relaxation delay [Figures 6b and 6a, respectively, of Muhandiram et al. (*23*)]. A diagram of secondary structural elements is provided at the top of the panel. (e) Residue-specific enhancement factors of cross-peaks in spectra of L99A recorded using CPMG-INEPT and free-precession INEPT $^{13}C$-$^1H$ HSQC schemes. Only large, positive values of $\eta_{CPMG}$ are shown, indicating exchange contributions to the $^1H$ line width. (f) Difference in methyl $^2H$ order parameter $S^2_{axis}$, $\Delta S^2$, for WT relative to L99A. Positive deviations from zero indicate increased flexibility for L99A relative to WT. Data for Ala$\beta$, Thr$\gamma$2, Met$\epsilon$, Ile$\gamma$2, Leu$\delta$1, and Val$\gamma$1 are shown in panels d–f at the appropriate residue number, whereas data for Ile$\delta$1, Leu$\delta$2, and Val$\gamma$2 are displaced by +0.5 unit along the *x*-axis. Note that $\Delta S^2$ values arise largely due to subtle changes in structure caused by the L99A mutation and cannot be interpreted as arising exclusively from differences in mobility between open and closed states since the closed conformation dominates in both WT and L99A (see text).

Exchange contributions to methyl $^1H$ spins can be investigated by comparing intensities observed in $^{13}C$-$^1H$ correlation spectra recorded using CPMG-HSQC and free-precession INEPT-based HSQC sequences. The enhancement factors obtained for the side chain methyl groups in L99A are presented in Figure 3e. Most peaks are slightly less intense in the CPMG-HSQC spectrum (by ~5%, negative values of $\eta_{CPMG}$ are not shown), but significant $R_{ex}(^1H)$ terms are clearly detected for Ile3$\gamma_2$, Met102$\epsilon$, Met106$\epsilon$, and Ala146$\beta$. Interestingly, there is not a 1:1 correlation between residues with significant values of $R_{ex}(^1H)$ and $R_{ex}(^{13}C)$. This is not surprising since a contribution from exchange is observed only in the case that there are significant chemical shift differences between exchanging sites. These results underscore the importance of using as large a number of different probes as possible to study dynamics.

Methyl side chain $^2$H relaxation rates were used to derive order parameters, $S^2_{axis}$, describing the amplitude of ps−ns time scale motions of the bond vector connecting the methyl carbon with its adjacent carbon (*23, 49*). The changes, $\Delta S^2_{axis}$, between WT and L99A [$S^2_{axis}$(WT) − $S^2_{axis}$(L99A)] are illustrated in Figure 3f. Residues were considered to have significant changes in order parameter only if (1) $\Delta S^2_{axis} > 2\sigma$, where $\sigma$ is the error in $\Delta S^2_{axis}$, and (2) $|\Delta S^2_{axis}| \geq 0.1$. The only significant changes in dynamics were all associated with increased flexibility in L99A, and were observed for Thr26$\gamma$2, Ile27$\delta$1, Leu33$\delta$2, and Thr34$\gamma$2 in the N-domain and Ile100$\delta$1, Val111$\gamma$2, and Ala129$\beta$ in the C-domain. This is shown in Figure 1c, where methyl groups with increased dynamics in L99A are colored in blue. It is important to note that in addition to the cavity mutation, L99A also differs from WT in that both cysteines in the protein have been replaced (C54T and C97A; see Materials and Methods). Thus, differences in side chain dynamics can originate from any one of the three mutations in L99A relative to WT, although in this regard it is noteworthy that changes in backbone dynamics were not observed between WT and the double mutant C54T/C97A. Interestingly, none of the methyl groups that have increased flexibility are within 6 Å of the sites of mutation, suggesting that the observed changes in ps−ns dynamics are the result of subtle changes in structure that are transmitted over long distances. This situation is to be contrasted with increased motions on the $\mu$s−ms time scale that were measured for L99A vs WT. These slow motions are localized almost completely to residues in proximity of the cavity (see above) and very likely are the result of an interconversion between a highly populated closed conformer and a much less abundant open state (see below). Unfortunately, correlations involving almost all of the methyl groups in the cavity region of L99A either were too weak to be observed (see above) or were not resolved in $^{13}$C-$^1$H correlation spectra. The exception is Ile78, for which both methyl pairs have the same level of dynamics in WT and L99A. It is therefore not possible to make conclusive statements about the extent of fast motions of methyls that are in direct contact with the cavity.

In combination, $^{15}$N and side chain $^2$H relaxation data indicate that fast dynamics are affected at relatively few positions in L99A vs WT and that these sites are remote from the cavity. In contrast, millisecond to microsecond time scale dynamics affect the relaxation properties for nuclei in the A-, E-, F-, G-, and I-helices in L99A, encompassing residues Ile3−Glu11, Ala99−Leu121, and Lys135−Thr142, but not in WT. Figure 1c highlights the regions of L99A affected by conformational exchange. Residues with backbone $^{15}$N spins with $R_{ex}$ are illustrated in green, while side chain methyls are indicated in green or orange, depending on whether exchange contributions were detected at methyl $^{13}$C or $^1$H positions, respectively. Clearly, the sculpting of a pocket inside the hydrophobic C-terminal domain of T4L has led to a loss of rigidity for many of the residues surrounding the cavity, manifest in the exchange between conformations on the millisecond to microsecond time scale.

Care must be used in the interpretation of these exchange contributions that report on dynamics at specific sites since the modulation of the shift of a spin (which gives rise to exchange) may be either a reflection of its own motion or, alternatively, the result of motion of some nearby atoms. For example, methyl groups of Met102, Met106, and Ala146 are within 5 Å of Trp138 of helix I, and the $^1$H line widths of these methyls show significant contributions from exchange (Figure 3e). Qualitative insight into the origin of the excess line widths can be obtained by comparing how the $^1$H and $^{13}$C line widths are affected. In the case of motion of a nearby aromatic such as Trp138, the range of shifts (in Hz) sampled by the neighboring methyl $^1$H spin is expected to be approximately a factor of 4 times larger than for the methyl $^{13}$C, and exchange contributions would thus be predicted to be larger for the $^1$H spin. A comparison of Figure 3d and Figure 3e shows that this is indeed what is observed for Met102 and Met106. In contrast, the vast majority of residues with backbone $^1$H or $^{15}$N spins within 5 Å of aromatic groups do not show any increased line width, and conversely those residues with backbone line width contributions from exchange are most often not proximal to aromatic side chains. In fact, Gly113 is the only nonaromatic residue within 5 Å of an aromatic side chain (Phe114) for which contributions to the $^1$H line width from $R_{ex}$ are observed, while nonaromatic residues that are proximal to aromatic side chains (≤5 Å) with contributions to $R_{ex}$($^{15}$N) include Arg8, Val111, Gly113, and Ile150. It is likely, therefore, that many of the residues for which $R_{ex}$ contributions are observed are in fact mobile on a $\mu$s−ms time scale.

Further insight into those residues that are most likely to be mobile on this time scale can be obtained from a consideration of crystallographic (*41*) and hydrogen exchange data (*50*), in addition to the above results. Specifically, helix F is likely to be dynamic when one considers that (1) it is intrinsically less stable than a typical helix because it is short and contains two glycines, (2) its backbone amides exchange rapidly with solvent (*50*), (3) it displays greater than average backbone and side chain disorder in the crystal (*40, 42*), and (4) a comparison of X-ray structures establishes that it moves in response to different ligands and becomes less ordered when binding oversized cavity ligands (*40*). Given that the substrate binding site is buried in the static structure of L99A (closed form), helix F may play an important role in creating a ligand-accessible pathway to the cavity, allowing for rapid access of these small molecules to the protein interior. While additional non-NMR data supporting significant amplitude motions of other helices for which $R_{ex}$ is observed are lacking, it may be that concerted motions of helices A, E, G, and I also occur in order to generate an open conformation, accessible to ligand.

*Rates of Protein Exchange Reported by $R_{ex}$($^{15}$N).* In the case of L99A, the large contributions to the $^{15}$N $R_2$ relaxation rates of the residues reported above can be interpreted in the context of a model in which these residues exchange between two sites resulting from protein isomerization. Such sites could well correspond to open and closed conformations of the protein which either allow or disallow ligand entry, for example. Under the assumption of a two-state process, the rate of site exchange can be obtained from the $^{15}$N $R_2$ relaxation rate dispersion in a CPMG experiment (*25, 31, 32*). Figure 4a shows $^{15}$N line widths of residues in L99A

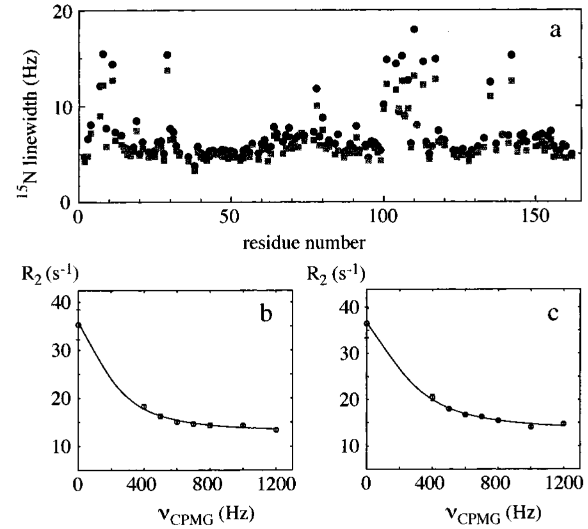

FIGURE 4: Quantitative analysis of intermediate time scale dynamics from $^{15}$N relaxation. (a) $^{15}$N line width measured in the free-precession limit from refocused, $F_1$-decoupled HSQCs recorded at 500 (gray squares) and 600 MHz (black circles) spectrometer field strength $B_o$. At 600 MHz, an increase of 0.4 Hz is observed for most residues along the backbone due to increased CSA relaxation, which is slightly larger than 0.3 Hz, expected on the basis of calculations for this protein. Larger deviations are seen for residues undergoing conformational exchange. In the limit of very fast exchange, the excess line width increases quadratically with $B_o$. Residues with $R_{ex}$(600 MHz) $\geq 10$ s$^{-1}$ arising from the creation of the cavity (see Figure 2f,g) and where $R_{ex}$ increases as $B_o^{\alpha}$ with $\alpha \geq 1.5$ (*56*), corresponding to $R_{ex}$(600 MHz)/$R_{ex}$(500 MHz) $> 1.3$, include Leu7, Arg8, Asn101, Phe104, Met106, Glu108, Gly110, Gly113, and Thr142. Panels b and c show $^{15}$N $R_2$ relaxation rate dispersion curves (500 MHz) as a function of rf field strength for residues Arg8 and Met106, respectively. Seven experimental points were obtained in the range 400−1200 Hz. The point at zero field corresponds to the free-precession limit (a). In the fitting procedure, a large uncertainty was assigned to this point, as it may contain contributions from static field inhomogeneity or incomplete decoupling (*34*).

measured in the free-precession limit in refocused, $F_1$-decoupled $^{15}$N-$^1$H HSQC spectra recorded at 500 and 600 MHz. The excess line width due to chemical exchange increases by more than 30% for a number of residues (see legend to Figure 4), which establishes that they are in "moderately fast exchange", $k_{ex} > \delta\omega$, where $\delta\omega$ is the chemical shift difference between the exchanging sites. Note that in the limit of very fast exchange, $R_{ex}$ is proportional to $B_o^2$, where $B_o$ is the spectrometer field strength (see Materials and Methods). The relaxation rate dispersion curves for these residues can therefore be fit with a two-site fast exchange model. Representative $^{15}$N $R_2$ relaxation profiles as a function of $B_1$ field for Arg8 and Met106 are shown in Figure 4b,c from which $k_{ex}$ values of 1490 s$^{-1}$ (Arg8) and 1820 s$^{-1}$ (Met 106) are obtained. All residues with large contributions to exchange resulting from formation of the cavity that are in the fast exchange limit have $k_{ex}$ values between 1270 and 1820 s$^{-1}$. It is also possible to obtain values for the factor $p_A p_B \delta\omega^2$ for each site with exchange (see Materials and Methods) from fits of the relaxation dispersion data. A minimum value on the order of 1 ppm is obtained for the shift difference between open and closed states; assuming a closed state population of $\geq$90% (see below), the average shift difference is $\geq$1.7 ppm.

*Binding of Xenon in the Cavity.* Chemical shift mapping was used to identify sites of interaction of xenon with L99A and to localize structural changes associated with ligand binding. The binding of Xe to the cavity results in small differences in chemical shift for the backbone nuclei with none larger than 0.2 ppm (rmsd shift changes of 0.03 ppm) or 0.8 ppm (rmsd of 0.2 ppm) for $^1$H and $^{15}$N, respectively, with the changes localized around the cavity. Larger changes (>1 ppm for $^{13}$C) were observed for the side chain methyl resonances of Val87$\gamma$1, Ala99$\beta$, Val111$\gamma$1, Leu118$\delta$2, and Leu121$\delta$1. These results indicate that xenon binds exclusively inside the cavity which is formed by the truncation of Leu99 and is accommodated by highly localized adjustments of a few side chains, with no significant effect on the structure of the protein backbone.

As discussed above, the binding of xenon quenches a large fraction of the exchange contributions observed in spectra of L99A (see Figures 2a−c and 3a−c). The decrease in $R_{ex}$ upon binding can be readily interpreted in terms of a shift in populations of the "open" and "closed" forms of the protein toward the closed state. This is consistent with the presence of saturating xenon resulting in increased packing of hydrophobic core residues and stabilization of the protein relative to free L99A (*40*). It is noteworthy that even in the absence of ligand L99A is predominantly closed. This follows from X-ray data showing that the structures of WT (closed conformation), L99A, and L99A+Xe are all superimposable [comparison of any two structures shows an rmsd of $\leq$0.2 Å for heavy atom backbone positions in the C-terminal domain of the protein (*27, 41, 42, 51*)], from NMR data where very few changes in backbone chemical shifts are noted between xenon-bound and free states (see Figure 2b,c) and from fits of the relaxation dispersion curves that indicate that minimum $^{15}$N shift differences between the open and closed states are on the order of 1 ppm (as described above). Such large differences in shifts between the two protein states would result in significant changes in chemical shifts between the ligand-bound, closed conformer and the ligand-free form if the free form of the protein were not heavily skewed toward the closed conformation as well (>90% closed).

The relaxation experiments recorded on L99A+Xe described above were completed within several days, and the xenon pressure was constant at 60 psi over this short time. Subsequently, the xenon pressure decreased gradually, and $^{13}$C-$^1$H correlation peaks which are sensitive to binding of xenon titrated to new positions as a function of the decreasing pressure. Movement of cross-peaks in this manner as a function of ligand indicates fast exchange of the ligand−protein complex. A qualitative estimate of the rate of interconversion between bound and free states can therefore be obtained from the largest chemical shift difference between the two states (300 Hz for Leu118$\delta_2$) corresponding to $k_{ex} \geq 1800$ s$^{-1}$. This value is somewhat larger than the off rates measured for indole and benzene, approximately 300 and 800 s$^{-1}$, respectively (*14*), likely the result of the smaller size of xenon relative to the two aromatic compounds and its corresponding lower affinity.

The ligand exchange process described above is linked with protein isomerization between open and closed protein states. This linked process can be described by a set of coupled reactions:

$$\mathrm{P{-}Xe} \underset{k_{-1}}{\overset{k_1}{\rightleftarrows}} \mathrm{P_O} + \mathrm{Xe} \qquad (1a)$$

$$\mathrm{P_O} \underset{k_{-2}}{\overset{k_2}{\rightleftarrows}} \mathrm{P_C} \qquad (1b)$$

where P−Xe, $\mathrm{P_O}$, and $\mathrm{P_C}$ are the xenon-bound, open, and closed states of L99A, respectively. Since $[\mathrm{P_C}] \gg [\mathrm{P_O}]$, the dissociation can be simplified further as

$$\mathrm{P{-}Xe} \underset{k_{-3}}{\overset{k_3}{\rightleftarrows}} \mathrm{P_C} + \mathrm{Xe} \qquad (1c)$$

The interconversion between $\mathrm{P_O}$ and $\mathrm{P_C}$ (eq 1b) occurs with a rate, $k_{ex} = k_2 + k_{-2} = 1500 \pm 200\ \mathrm{s}^{-1}$, established from the $B_1$ field dependence of the excess $^{15}$N line width (Figures 4b,c), while a qualitative estimate of $k_3 + k_{-3}[\mathrm{Xe}] \sim 1800\ \mathrm{s}^{-1}$ (xenon pressure of 60 psi) is based on the chemical shift vs pressure dependence of cross-peaks from methyl groups near the cavity.

*Dynamics Are Critical for Rapid Ligand Binding to L99A.* It is clear from the high-resolution structure of L99A that if the protein were completely static access of ligand would not be possible. Moreover, an extremely large activation barrier would have to be overcome if passage of ligand to the cavity were accompanied by a breaking of all the protein interactions along the binding pathway in the case of a static structure which rapidly switches from ligand-free to -bound states. In contrast, a protein exchanging between open and closed states involving helices E, F, G, and I (see Figure 1c) could allow rapid ligand access. In this scenario, the loss in protein stability from reduction in enthalpic contributions in a dynamic system would be compensated by an increase in entropy. For T4 lysozyme, the changes relative to the wild-type protein in the standard free energy of unfolding upon single cavity mutations [$\Delta\Delta G_{\mathrm{unfolding}} = \Delta G_{\mathrm{unfolding(cavity)}} - \Delta G_{\mathrm{unfolding(WT)}}$] vary between −5 and 0 kcal/mol (44 °C) and are to good approximation linear with cavity size (*35*, *38*). In contrast, the associated changes in the enthalpy of unfolding cover a much wider range ($\Delta\Delta H_{\mathrm{unfolding}}$ between −20 and −2 kcal mol$^{-1}$) and appear unrelated to cavity size (*52*). These results suggest that cavity formation which destabilizes the protein enthalpically is accompanied by a significant increase in entropy, which compensates to a large extent for the enthalpy change. In the case of L99A, the present study indicates that the partial loss of the closely packed core promotes extensive $\mu$s−ms time scale dynamics of both protein side chain and backbone atoms. Enthalpy and entropy are closely balanced in the process, and the emergence of a highly flexible portion of the molecule occurs at low free energy cost. This study also localizes the regions of L99A that show increases in dynamics in response to cavity formation and that are ultimately likely to be involved in establishing the path for ligand entry. It is noteworthy that removal of ligands or cofactors from other proteins such as flavodoxin (*53*) and intestinal fatty acid binding protein (*54*) results in a concomitant increase in $\mu$s−ms time scale dynamics, in a manner similar to what is observed in the case of L99A upon removal of xenon. Thus, the role of dynamics in compensating for the loss of favorable ligand−protein interactions while at the same time "priming" the molecule for rapid binding is likely to be a common feature in many ligand-binding proteins.

## ACKNOWLEDGMENT

We thank Christopher Bertole and Charles Mims (University of Toronto) for supplying the xenon used in the present study and Dr. Art Palmer (University of Columbia, New York) for providing the programs Quadric1.11 and Modelfree4.0 used in the analysis.

## REFERENCES

1. Gurd, F. R. N., and Rothgeb, M. (1979) *Adv. Protein Chem. 33*, 73−165.
2. Huber, R. (1979) *Trends Biochem. Sci. 4*, 271−276.
3. Alber, T., Gilbert, W. A., Ringe, D., and Petsko, G. A. (1983) *Ciba Found. Symp. 93*, 4−24.
4. Frauenfelder, H., Parak, F., and Young, R. D. (1988) *Annu. Rev. Biophys. Biophys. Chem. 17*, 451−479.
5. Karplus, M., and Petsko, G. A. (1990) *Nature 347*, 631−639.
6. Frauenfelder, H., Sligar, S. G., and Wolynes, P. G. (1991) *Science 254*, 1598−1603.
7. Yon, J. M., Perahia, D., and Ghélis, C. (1998) *Biochimie 80*, 33−42.
8. Karplus, M. (1986) *Methods Enzymol. 131*, 283−307.
9. Wagner, G., and Wüthrich, K. (1986) *Methods Enzymol. 131*, 307−326.
10. Palmer, A. G. (1997) *Curr. Opin. Struct. Biol. 7*, 732−737.
11. Jardetzky, O. (1998) in *Protein Dynamics, Function and Design* (Jardetzky, O., and Lefevre, J.-F., Eds.) pp 103−127, Plenum Press, New York.
12. Kay, L. E. (1998) *Nat. Struct. Biol., NMR Suppl. 5*, 513−516.
13. Fersht, A. (1985) *Enzyme Structure and Mechanism*, 2nd ed., Freeman & Co., New York.
14. Feher, V. A., Baldwin, E. P., and Dahlquist, F. W. (1996) *Nat. Struct. Biol. 3*, 516−521.
15. Matsumura, M., Becktel, W. J., and Matthews, B. W. (1988) *Nature 334*, 406−410.
16. Sattler, M., Schleucher, J., and Griesinger, C. (1999) *Prog. Nucl. Magn. Reson. 34*, 93−158.
17. McIntosh, L. P., Wand, A. J., Lowry, D. F., Redfield, A. G., and Dahlquist, F. W. (1990) *Biochemistry 29*, 6341−6362.
18. Fischer, M. W. F., Majumdar, A., Dahlquist, F. W., and Zuiderweg, E. R. P. (1995) *J. Magn. Reson., Ser. B 108*, 143−154.
19. Gardner, K. H., Zhang, X., Gehring, K., and Kay, L. E. (1998) *J. Am. Chem. Soc. 120*, 11738−11748.
20. Bax, A., Max, D., and Zax, D. (1982) *J. Am. Chem. Soc. 114*, 6923−6925.
21. Neri, D., Szyperski, T., Otting, G., Senn, H., and Wüthrich, K. (1989) *Biochemistry 28*, 7510−7516.
22. Farrow, N. A., Muhandiram, R., Singer, A. U., Pascal, S. M., Kay, C. M., Gish, G., Shoelson, S. E., Pawson, T., Forman-Kay, J. D., and Kay, L. E. (1994) *Biochemistry 33*, 5984−6003.
23. Muhandiram, D. R., Yamazaki, T., Sykes, B. D., and Kay, L. E. (1995) *J. Am. Chem. Soc. 117*, 11536−11544.
24. Mulder, F. A. A., Spronk, C. A. E. M., Slijper, M., Kaptein, R., and Boelens, R. (1996) *J. Biomol. NMR 8*, 223−228.
25. Mulder, F. A. A., van Tilborg, P. J. A., Kaptein, R., and Boelens, R. (1999) *J. Biomol. NMR 13*, 275−288.
26. Delaglio, F., Grzesiek, S., Vuister, G. W., Zhu, G., Pfeifer, J., and Bax, A. (1995) *J. Biomol. NMR 6*, 277−293.
27. Eriksson, A. E., Baase, W. A., and Matthews, B. W. (1993) *J. Mol. Biol. 229*, 747−769.
28. Lee, L. K., Rance, M., Chazin, W. J., and Palmer, A. G. (1997) *J. Biomol. NMR 9*, 287−298.
29. Mandel, A. M., Akke, M., and Palmer, A. G. (1995) *J. Mol. Biol. 246*, 144−163.
30. Lipari, G., and Szabo, A. (1982) *J. Am. Chem. Soc. 104*, 4546−4559.
31. Orekhov, V. Y., Pervushin, K. V., and Arseniev, A. S. (1994) *Eur. J. Biochem. 219*, 887−896.
32. Luz, Z., and Meiboom, S. (1963) *J. Chem. Phys. 39*, 366−370.

33. Shaka, A. J., Lee, C. J., and Pines, A. (1988) *J. Magn. Reson. 77*, 274−293.
34. Akke, M., Liu, J., Cavanagh, J., Erickson, H. P., and Palmer, A. G. (1998) *Nat. Struct. Biol. 5*, 55−59.
35. Eriksson, A. E., Baase, W. A., Zhang, X.-J., Heinz, D. W., Blaber, M., Baldwin, E. P., and Matthews, B. W. (1992) *Science 255*, 178−183.
36. Matthews, B. W. (1993) *Annu. Rev. Biochem. 62*, 139−160.
37. Matthews, B. W. (1995) *Adv. Protein Chem. 46*, 249−278.
38. Xu, J., Baase, W. A., Baldwin, E., and Matthews, B. W. (1998) *Protein Sci. 7*, 158−177.
39. Eriksson, A. E., Baase, W. A., Wozniak, J. A., and Matthews, B. W. (1992) *Nature 355*, 371−373.
40. Morton, A., and Matthews, B. W. (1995) *Biochemistry 34*, 8576−8588.
41. Weaver, L. H., and Matthews, B. W. (1987) *J. Mol. Biol. 193*, 189−199.
42. Wray, J. W., Baase, W. A., Lindstrom, J. D., Weaver, L. H., Poteete, A. R., and Matthews, B. W. (1999) *J. Mol. Biol. 292*, 1111−1120.
43. Mueller, L., Legault, P., and Pardi, A. (1995) *J. Am. Chem. Soc. 117*, 11043−11048.
44. Johnson, C. S., Jr. (1965) *Adv. Magn. Reson. 1*, 33−102.
45. Woessner, D. E. (1962) *J. Chem. Phys. 36*, 1−4.
46. Zhang, X.-J., Wozniak, J. A., and Matthews, B. W. (1995) *J. Mol. Biol. 250*, 527−552.
47. van Tilborg, P. J. A., Mulder, F. A. A., de Backer, M. M. E., Nair, M., van Heerde, E., Folkers, G., van der Saag, P. T., Karimi-Nejad, Y., Boelens, R., and Kaptein, R. (1999) *Biochemistry 38*, 1951−1956.
48. Ishima, R., Wingfield, P. T., Stahl, S. J., Kaufman, J. D., and Torchia, D. A. (1998) *J. Am. Chem. Soc. 120*, 10534−10542.
49. Kay, L. E., Muhandiram, D. R., Farrow, N. A., Aubin, Y., and Forman-Kay, J. D. (1996) *Biochemistry 35*, 361−368.
50. Llinas, M., Gillespie, B., Dahlquist, F. W., and Marqusee, S. (1999) *Nat. Struct. Biol. 6*, 1072−1078.
51. Quillin, M. L., Breyer, W. A., Griswold, I. J., and Matthews, B. W. (2000) *J. Mol. Biol.* (in press).
52. Connely, P., Ghosaini, L., Hu, C.-Q., Katamura, S., Tanaka, A., and Sturtevant, J. M. (1991) *Biochemistry 30*, 1887−1891.
53. Steensma, E., and van Mierlo, C. P. (1998) *J. Mol. Biol. 282*, 653−666.
54. Hodsdon, M. E., and Cistola, D. P. (1997) *Biochemistry 36*, 2278−2290.
55. Koradi, R., Billeter, M., and Wüthrich, K. (1996) *J. Mol. Graphics 14*, 51−55.
56. Millet, O., Loria, J. P., Kroenke, C. D., Pons, M., and Palmer, A. G. (2000) *J. Am. Chem. Soc. 122*, 2867−2877.

BI001351T